Review

Rare-earth ion doped Al_2O_3 for active integrated photonics

Ward A. P. M. Hendriks, Lantian Chang, Carlijn I. van Emmerik, Jinfeng Mu, Michiel de Goede, Meindert Dijkstra, Sonia M. Garcia-Blanco*

Optical Sciences, MESA+ Institute for Nanotechnology, University of Twente, 7500 AE Enschede, The Netherlands; ostnw@utwente.nl
*s.m.garciablanco@utwente.nl

Abstract: Aluminum oxide (Al_2O_3) is an emerging material in integrated photonics. It exhibits a very broad transparency window from the UV to the mid-IR, very low propagation losses and a high solubility for rare-earth ions leading to optical gain in different spectral ranges. Al_2O_3 can be deposited by different wafer-level deposition techniques, including atomic layer deposition and reactive magnetron sputtering, being compatible with the monolithic integration onto passive integrated photonics platforms, such as Si_3N_4, to which it provides optical amplification and lasing. When deposited at low temperatures, it is also compatible with integration onto CMOS chips. In this review, the state-of-the-art on the deposition, integration and device development in this photonic platform is described.

Keywords: Integrated photonics, aluminum oxide, Al_2O_3, rare-earth ions, on-chip amplifier, on-chip laser

---

1. Al_2O_3 as a material for integrated photonics

Aluminum oxide (Al_2O_3) is a dielectric material found in both crystalline and amorphous phases. It has attractive features making it an excellent candidate for integrated photonic devices. Al_2O_3 exhibits a wide transparency window extending from the ultraviolet to the mid-infrared (150—5500 nm) [1]. Optical waveguiding has been shown in amorphous Al_2O_3 at various wavelengths within its transparency window, including waveguides and devices at 371 nm [2], 1020 nm [3], 1550 nm [4,5,6,7] and 2000 nm [8]. Low optical losses down to 0.1±0.02 dB/cm [9, 10] and 0.04±0.02 dB/cm in the C-band [11] have been demonstrated for planar slab waveguides deposited by reactive sputtering and atomic layer deposition, respectively. After waveguide definition with reactive ion etching, propagation losses below 0.2 dB/cm have been demonstrated at a wavelength of 1550 nm [6, 9]. In addition, Al_2O_3 possesses a refractive index contrast of ~0.2 with the SiO_2 cladding, which allows for a relatively dense integration of optical functions on-chip, with bend radii down to tens of micrometers [12-14]. Al_2O_3 can be readily deposited on full wafers allowing for wafer-scale processing compatible with silicon photonics technologies.

Al_2O_3 has a trivalent rare-earth ion solubility [15] higher than other silicon-based photonic material platforms [16-17] and silica-based glasses [18, 19], which allows for active functionalities when the material is doped with different rare-earth ions. Amplification and lasing have been demonstrated at a variety of wavelengths, including ~0.88, ~1.06 and ~1.33 μm for Nd^{3+}:Al_2O_3 [20], ~1.03 μm for Yb^{3+}:Al_2O_3 [3, 12, 13, 21-22], ~1.55 μm for Er^{3+}:Al_2O_3 [7, 9, 12, 13 15, 23-43], ~1.8-1.9 μm for Tm^{3+}:Al_2O_3 [44-45] and at ~2 μm for Ho^{3+}:Al_2O_3 [8].

Rare-earth ion doped Al_2O_3 has been used in the last few decades for the realization of on-chip amplifiers [9, 7, 15, 20, 23-28, 46] and lasers [8,10, 12, 15, 18, 19, 21, 22, 30-45] that exhibited ultra-narrow linewidths down to 1.7 kHz [31], broad tunability [39] and relatively high output power [41,

45]. Its monolithic integration with different passive photonic integration platforms, including Si_3N_4 [8, 10, 12-14, 27, 33-45], undoped Al_2O_3 [47] and SOI [48-50] paves the way towards scalable active-passive photonic chips, in which all the required sources and amplifiers are monolithically integrated, therefore reducing the complexity of current active-passive assembly methods [51].

In this review, we first give an overview of the most used techniques for the deposition of rare-earth ion doped Al_2O_3. We then review the approaches that have been explored for the integration of Al_2O_3 to both SOI and silicon nitride. An overview of developed devices realized both completely on Al_2O_3 as well as on Al_2O_3 integrated onto a passive platform, will be given. We divide the devices section into amplifiers and lasers, independently of the application field and of the rare-earth ion used as dopant. The review focuses on the developments undertaken during the last decade.

2. Deposition of optical quality Al_2O_3 layers

Al_2O_3 can be deposited using a variety of methods including synthesis by the sol-gel method [52-57], chemical vapor deposition (CVD) [58, 59], pulsed laser deposition (PLD) [60-65], atomic layer deposition (ALD) [11, 27, 66-74] and reactive sputtering [3-10, 12-16, 20-22, 26, 29-41, 44-45, 75-85]. The layers made by sol-gel and CVD suffer from high passive losses and luminescence quenching due to OH- incorporation into the host material. This probably accounts for the lack of publications reporting devices based on channel waveguides using these materials. The layers deposited by PLD exhibit propagation losses of typically ~2.5 dB/cm at 632 nm [62]. Very low propagation losses, below 0.4 dB/cm at 633 nm, have been reported for films deposited by both atomic layer deposition and reactive sputtering [2, 12]. These two deposition methods will be reviewed in more detail in the following subsections.

2.1. Atomic layer deposition of optical quality Al_2O_3 layers

Atomic layer deposition (ALD) is a chemical vapor deposition technique in which alternating gas precursors are flown over the substrate reacting with their surface in a self-terminating way, thereby growing a thin film [68-74]. In between gases, a purging step is applied to eliminate any unreacted species before the start of the next cycle. The precursors utilized in ALD are always flown independently, in contrast with other chemical vapor deposition techniques. An ALD cycle consists of a series of sequential reactant-purge steps (Figure 1). Each reactant-purge step constitutes a half-cycle. One of the advantages of ALD is the control over the deposition rate, which can be as accurate as the thickness of a half-cycle. The sub-monolayer control over the deposition allows engineering the deposited material to, for example, control the separation of rare-earth ion dopants to limit luminescence quenching effects that limit the achievable gain [27, 74]. The great control over the deposition permits to achieve a great degree of conformality, allowing to fill in very small gaps, which has been exploited in slot-waveguide configurations such as the one shown in Figure 1. However, since each cycle typically produces a thickness on the order of 1-1.2 Å, deposition of micrometer thick layers requires very long deposition times.

The deposition of Al_2O_3 films by atomic layer deposition is one of the most well-known processes in the semiconductor industry. The most used precursors for this process are trimethylaluminum (TMA) and water (H_2O). Nitrogen purging is usually reported for up to 8 sec per purge [66]. Deposition temperatures between 150 and 300 C have been investigated and the effect of the deposition temperature on the quality, i.e., refractive index and crystallinity, of the deposited layers has been reported [68]. The refractive index increased from 1.629 to 1.639 at a wavelength of 1550 nm for layers deposited at 150 C and 300 C, respectively. All layers were predominantly amorphous with only the layers deposited at 300 C exhibiting the signature of amorphous α- and γ-Al_2O_3 in its XRD spectrum. Losses below 0.1 dB/cm were measured in slab waveguides from 632.8 nm till 1550 nm for the film deposited at 300 C. Both Alsan *et. al.* [66] and West *et. al.* [2] deposited their Al_2O_3 films using

ALD at 300 C, reporting similar refractive indices and slab losses. Channel waveguide losses below 3 dB/cm at 400 nm were reported by West *et. al*. [2] showing the potential of this material for broad bandwidth applications down to the UV. Rönn *et. al*. showed that annealing above 600 C increases the luminescence of the films when doped with erbium. However, as the annealing temperature is increased above 800 C, a polycrystalline γ -Al_2O_3 phase starts forming, which leads to high propagation losses (>20 dB/cm) [2]. An annealing temperature of 750 C was the optimum selected by Rönn *et. al.* to achieve the maximum photoluminescence of the rare-earth ions with minimum losses [27,43].

ALD permits engineering the deposited layers by controlling the composition of each ALD cycle. In that way, the optical, electronic and morphological properties can be controlled by adjusting either the bilayer thickness or the relative thicknesses of the layers in the stack [71]. Al_2O_3-Y_2O_3 multilayers were investigated for integrated optical waveguides with tailorable bandgap [71]. Al_2O_3-Er_2O_3 multilayers were studied to maximize optical gain for on-chip amplification in the C-band [27-28, 74]. Al_2O_3-ZnO multilayers were exploited to produce highly non-linear optical waveguides [86, 87].

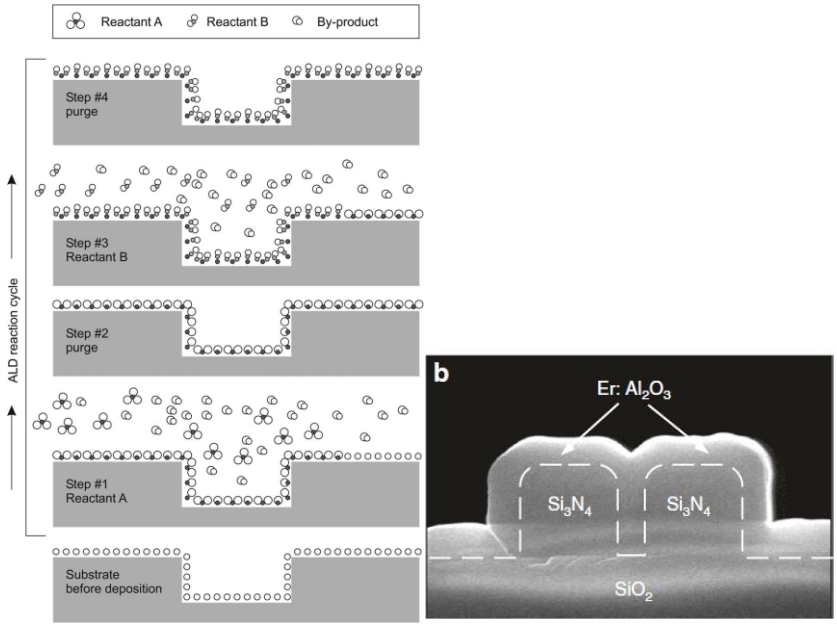

Figure 1. (a) Schematic of the atomic layer deposition process. One ALD-cycle consists of steps #1-#4. Figure taken from [69]. (b) SEM photograph of a slot waveguide in Si_3N_4 showing a conformal coating of Er^{3+}:Al_2O_3 to achieve a highly efficient on-chip amplifier. A gain per unit length of 20 dB/cm was measured. Picture taken from [27].

2.2. Reactive magnetron sputtering of optical quality Al_2O_3 films

Reactive magnetron sputter deposition of Al_2O_3 is based on the sputtering of metallic aluminum (Al) from a target that subsequently undergoes a chemical reaction with the reactive gas, in this case O_2, on the substrate and walls of the reaction chamber to deposit an Al_2O_3 layer. Inert argon ions are generally used to sputter the aluminum atoms from the target. During the sputtering process not only aluminum atoms are released from the target but also secondary electrons. An electric potential (i.e., bias voltage) between the target and the chamber wall, which acts respectively as cathode and anode, attracts the argon ions to the target. The emitted electrons become energized and are accelerated away from the target ionizing the neutral argon gas. A strong bended magnetic field on the target surface traps the electrons close to the target to enhance the overall sputtering yield. DC reactive sputtering suffers from continued localized charge build up when the target is partially oxidized, with the consequent reduction in optical quality of the deposited layers due to arcing [75].

RF reactive sputtering has been demonstrated to lead to high optical quality layers with low optical propagation losses. Optical propagation losses of undoped Al_2O_3 slab waveguides below 0.4 dB/cm at 633 nm have been reported [12]. After etching, channel waveguides with typically less than 0.2 dB/cm at 1550 nm have been fabricated [6, 9].

The optical and morphological properties of the sputtered layers depend largely on the deposition parameters, including the substrate temperature, oxidation state of the sputtering target and impact of energetic species on the substrate. The bias voltage can be measured as a function of oxygen flow or oxygen partial pressure in the chamber to determine the oxidation state of the target [88-89]. The sputtering mass deposition rate is directly related to the oxidation state of the target since metallic aluminum has a higher sputtering yield than oxidized aluminum (i.e., alumina) [89]. An oxidized target exhibits also higher secondary electron emission and sputtering of negative species such as O^-, which are accelerated towards the substrate and add energy to the deposited material affecting its morphology [90, 91]. Figure 2 shows a typical bias curve for RF reactive sputtering of Al_2O_3. For low oxygen flows, the target is fully metallic (i.e., zone 1). The sputtered aluminum reacts with the O_2 on the chamber walls and substrate to produce Al_2O_3 (i.e., "gettering"). The argon bombardment on the target keeps it "clean" from formation of an Al_2O_3 layer. As the O_2 flow increases within Zone 1, the bias voltage stays stable and the oxygen partial pressure remains stable for increasing oxygen flow into the chamber. After a certain O_2 flow, known as the "knee point" or "sputtering knee point", the gettering capacity of the walls and substrate saturates and the oxygen partial pressure starts increasing with an increased oxygen flow. The excess O_2 in the chamber contributes to an increase of the oxidation of the target. Since the argon flow is constant, the argon bombardment is not sufficient to keep a metallic target by removing the oxidation on the target surface. Partial oxidation of the target starts, with an increase of secondary electron emission due to the higher secondary emission yield of oxidized aluminum. Keeping a constant power results in a drop of the bias voltage (i.e., zones 2 and 3 in Fig. 2). The deposition rate drops due to a lower sputtering yield of Al_2O_3 versus Al and a decreased discharge voltage, reducing the incident energy of the argon ions on the target. This is a self-reinforcing loop that converges to the right side of the bias curve (i.e., zone 4), in which the target is fully oxidized ("poisoned") and the deposition rate is significantly decreased. This process can exhibit hysteresis [92], which prevents achieving an optimal and stable process in the transition region (i.e., zones 2-3) of the bias curve [91]. Bobzin *et. al.* reported the different material structures expected for depositions in the different zones of the bias curve. A full description of morphological zones as a function of deposition parameters can be found in [90]. By controlling the oxidation state of the sputtering target, Al_2O_3 layers with the desired morphology could be deposited in a reproducible manner with high optical quality [76].

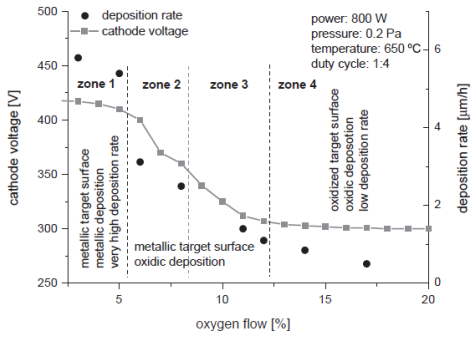

Figure 2. Cathode voltage (also known as bias voltage) versus oxygen flow in the reaction chamber (left axis) and deposition rate as a function of oxygen flow (right axis). Different zones are indicated, namely the zone 1, which corresponds to a metallic target and deposition of not fully oxidized aluminum, zones 2 and 3, corresponding to a metallic target and fully oxidized layers, and zone 4, which corresponds to an oxidized ("poisoned") target. Figure taken from [91].

The Al_2O_3 can be doped by using a second target [7,9]. As already mentioned before, Yb^{3+}, Nd^{3+}, Er^{3+}, Tm^{3+} and Ho^{3+} have already been utilized in practical devices. The influence of doping concentration, in particular of thulium, on the refractive index of RF reactive co-sputtered Al_2O_3 has been reported by Loiko *et. al.* [93].

Typically, reported deposition temperatures are relatively elevated (i.e., above 450 C). The high temperature limits the type of substrates over which the material can be deposited. By applying a voltage to the substrate, excellent guiding(i.e., losses ~0.1 dB/cm at 1550 nm) Al_2O_3 slab waveguides were deposited at 250 C [37]. In that study, 90 V was the maximum voltage that could be applied to the substrate. The combination of 90 V bias to the substrate and 250 C led to the best guiding layers. Higher or lower temperature both drastically increased the propagation losses, likely due to nano-crystallinity and cluster-void formation in the layer respectively. By controlling the energy of the aluminum atoms arriving to the surface of the substrate by a combination of bias voltage and temperature, different layer morphologies were obtained [90].

3. Monolithic integration of Al_2O_3 onto passive photonic platforms

The complexity of the integrated photonic chips realized in silicon photonics technology, including the silicon-on-insulator (SOI) and the silicon nitride (Si_3N_4) platforms, is steadily increasing. However, these photonic integration platforms do not possess the capability of light generation/amplification (i.e., optical gain). To achieve active devices such as lasers and amplifiers, active gain materials are normally integrated into these passive platforms, typically via hybrid or heterogeneous integration scheme [51]. Monolithic integration of rare-earth ion doped Al_2O_3 onto these platforms shows promising potential towards the manufacturable integration of optical gain materials onto the passive photonic integration platforms without additional non-scalable complex assembly steps. Furthermore, the integration of the laser pump source by butt coupling [51], grating coupling (i.e., VCELS flip-chip bonding [94]) or by heterogeneous integration [95] does not impose stringent requirements as it does not form part of the device cavity . In the following subsections, the different integration schemes of rare-earth ion doped Al_2O_3 onto both the SOI and silicon nitride platforms will be reviewed.

3.2. Integration of rare-earth ion doped Al_2O_3 onto SOI

The monolithic integration of Er^{3+}:Al_2O_3: onto the SOI platform towards the realization of on-chip optical amplifiers in this platform was first demonstrated by sputtering an Er^{3+}:Al_2O_3 layer on the top of SOI waveguides [96]. Adiabatic waveguides width tapers were used to couple the light from the silicon waveguides to the ridge erbium doped Al_2O_3 waveguides, as shown in Figure 3 (a). A signal enhancement of 7 dB (i.e., ratio of the output power through the device with the pump on and off) was experimentally demonstrated after pumping with 1480 nm light. In that study, optical gain was not achieved due to the very elevated propagation losses of the device [96].

In a theoretical study, Pintus *et. al.* suggested inserting heavily Er^{3+} doped Al_2O_3 into a silicon slot waveguide to achieve emission at 2.8 μm, which would be very useful for optical sensing and spectroscopy [42]. Recently, erbium doped Al_2O_3 was utilized as cladding to silicon microring resonators [49] and silicon photonic molecules [50] to reduce the losses and therefore increase the Q-factors (Figure 3 (b)).

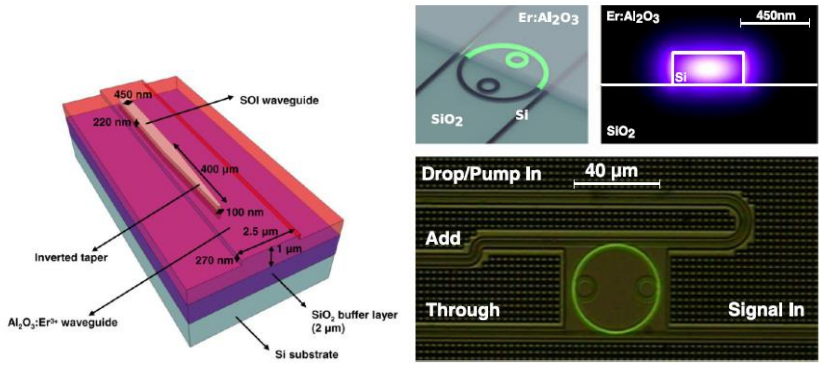

Figure 3. (a) Erbium doped Al_2O_3-SOI device showing the inverted tapers to transfer the mode from the SOI to the Al_2O_3 waveguide. Taken from [96]. (b) Use of erbium doped Al_2O_3 to reduce the losses, thereby increasing the Q-factor, of SOI ring resonators and photonic molecules. Taken from [49].

3.2. Integration of rare-earth ion doped Al_2O_3 onto Si_3N_4

Recent efforts have been directed towards the integration of rare-earth ion doped Al_2O_3 to the passive silicon nitride platform. Bradley *et. al*. proposed an integration scheme in which the doped Al_2O_3 material was sputtered into trenches etched on the SiO_2 cladding deposited on top of segmented Si_3N_4 waveguides [12], as shown in Figure 4 (a). The advantage of this integration scheme is that it eliminates the need for performing reactive ion etching of the Al_2O_3 material, which together with the Si_3N_4 waveguides underneath forms a hybrid mode. The concept was further developed in [14, 44] by depositing Al_2O_3 into a trench etched into the SiO_2 cladding without silicon nitride waveguides underneath, Figure 4 (b). The Al_2O_3 rings are coupled to Si_3N_4 bus waveguides. This integration scheme has been applied mostly to devices where bends are needed. In those devices, only the microring contains the doped Al_2O_3 gain material while the bus waveguide is fully passive. In [39], an adiabatic taper is designed to make a low loss transition, ~0.3 dB/cm loss, between the Si_3N_4 and doped Al_2O_3 waveguides. For straight devices, such as distributed feedback lasers (DFB) and distributed Bragg reflector (DBR) lasers, the doped Al_2O_3 layer can be simply deposited on top of the Si_3N_4 waveguides both multi-[8, 35, 36, 45] or single-striped [33, 40, 41] (Figure 5 (a)). A hybrid mode is then formed with close to 90 % mode overlap with the doped Al_2O_3 oxide region and between pump and laser modes (Figure 5 (b)). The reported devices to date are fully doped. The integration with passive optical functions in silicon nitride are enabled thanks to the development of suitable couplers to produce a low-loss transition between the hybrid mode and the Si_3N_4 mode [77].

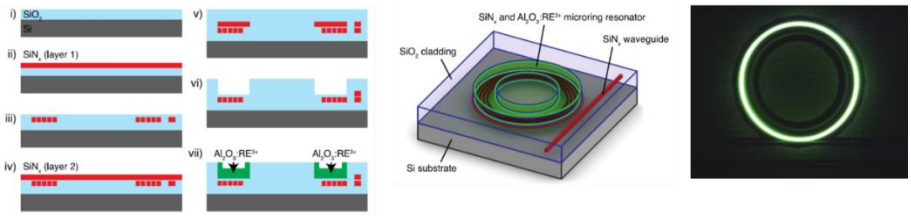

Figure 4. (a) Silicon-compatible microring laser fabrication steps. (b) Illustration of the resulting monolithic rare-earth ion doped microring laser structure. Figure taken from [12].

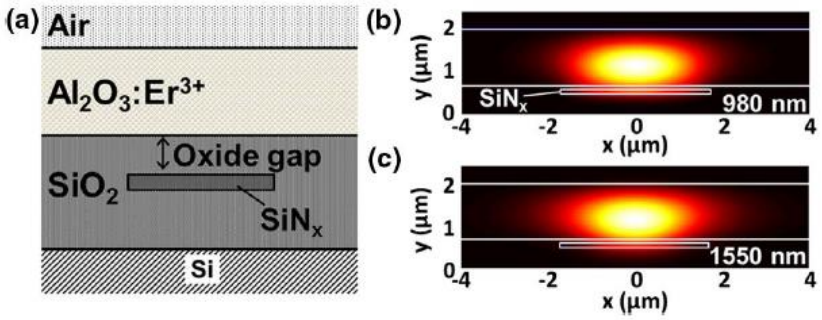

Figure 5. (a) Schematic of an Al_2O_3-Si_3N_4 waveguide cross-section in which the Si_3N_4 is a single stripe. (b) and (c) Simulations of the optical mode at the pump and signal wavelengths showing good overlap (~90 %) with the active gain material. Figure taken from [33].

A double layer photonic platform has been proposed, in which Si_3N_4 waveguides and rare-earth ion doped Al_2O_3 waveguides lie in two different photonic layers separated by a SiO_2 spacer layer. The transition between the bottom Si_3N_4 and top Al_2O_3 waveguides is done by means of low-loss adiabatic couplers in which the thickness of the Si_3N_4 waveguides is vertically tapered to circa 30 nm. Figure 6 (a) shows the 3D, top view and side view schematics of the couplers as well as the cross-sections at different positions along the length of the coupler. Transition losses below 0.2 dB/coupler were experimentally demonstrated [78, 79]. The couplers exhibited very high tolerance to lateral misalignment (~±2 μm for 1 dB penalty for wavelengths in the C-band) during the lithography step of the top photonic layer. On chip amplifiers [80] and microring lasers [81] have been demonstrated using this approach. Figure 6 (b) shows and example of a zigzag Si_3N_4 waveguide integrated with several sections of Er^{3+}:Al_2O_3, where the green light is generated by energy transfer upconversion under 980 nm wavelength pumping.

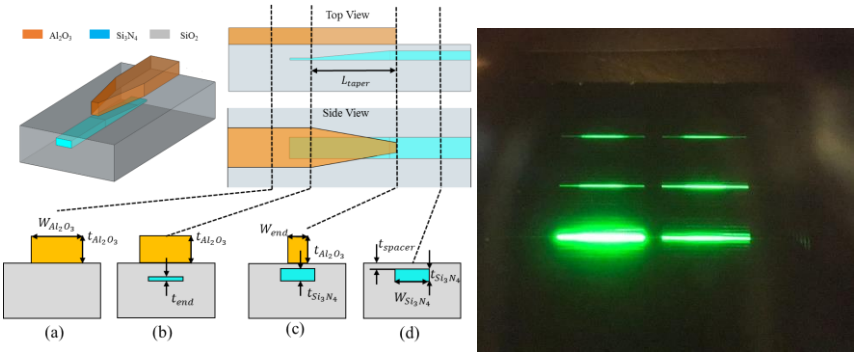

Figure 6. (a) 3D schematic of the adiabatic vertical coupler showing the cross-section at different longitudinal positions along the coupler. Figure taken from [78]. (b) Series of active (Er^{3+}: Al_2O_3)-passive (Si_3N_4) sections.

A single layer integration scheme has also been proposed and experimentally demonstrated for active on passive Al_2O_3 integration [47]. The process is illustrated in Figure 7 (a). An ytterbium doped Al_2O_3 layer is sputtered through a shadow mask followed by the deposition of undoped Al_2O_3 and subsequent planarization by CMP. A single lithographic step defines the passive-active devices simultaneously. Unfortunately, no amplifiers or lasers have been yet demonstrated using this approach, only the demonstration of the proof-of-concept of the integration process.

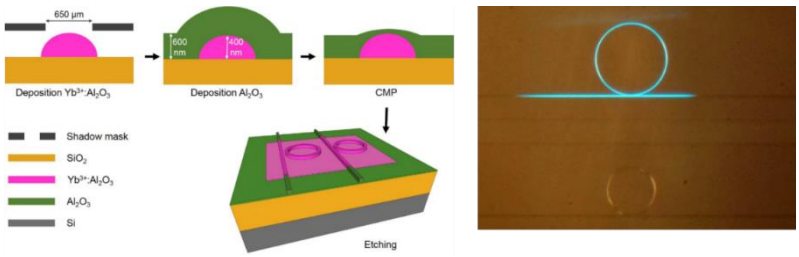

Figure 7. Schematic of the process flow for the integration of active-passive Al_2O_3 on a single layer. (b) Demonstration of the integration scheme. Figure taken from [47].

Recently, erbium doped Al_2O_3 lasers integrated with Si_3N_4 waveguides were introduced onto a CMOS compatible silicon photonic platform to produce a fully integrated system-on-a-chip [77, 97].

4. On-chip amplifiers in Al_2O_3.

Since the invention of the erbium doped fiber amplifier in the late 80's [98], EDFA's have become key components in many telecommunication systems. Fiber amplifiers doped with different rare-earth ions including Yb^{3+} (YDFA) [99], Nd^{3+} [100], Er^{3+} [101] and Tm^{3+} [102] can enable applications covering the wavelength ranges near the 1 µm, 1.3 µm, 1.5 µm and 2 µm bands. Advantages of rare-earth ion doped amplifiers include the broad gain bandwidth provided by these ions, the intrinsically low noise and the capability to amplify high-bit-rate signals. This is mainly due to their long excited state lifetime and their compatibility with the rest of the fibers in the system.

Integrated photonic waveguides increase the mode field intensity, leading to a more efficient interaction between the pump photons and active ions. Furthermore, the higher refractive index contrast in integrated photonic platforms with respect to optical fibers leads to smaller devices. Rare-earth ion doped waveguide amplifiers have been the subject of much research over the last few decades with many host materials for the rare-earth ions being investigated. A very complete review can be found in [15]. The requirements for a good material platform for the realization of rare-earth ion doped waveguide amplifiers include a high rare-earth ion solubility, deposition at the wafer level, and low passive propagation loss. From all the materials studied [15], Al_2O_3 appears as a good candidate due to the high solubility for rare-earth ions, a refractive index of 1.65-1.73 varied by doping, and passive losses of less than 0.1 dB/cm at 1550 nm of wavelength. The spectroscopy of rare-earth ions and, in particular, of rare-earth ions doped in Al_2O_3 has been the subject of many previous reports [103-106]. In the following paragraphs, the rare-earth-ion doped Al_2O_3 amplifiers and its integration with other passive platforms in the last decade will be reviewed. Their achieved parameters will be introduced, such as maximum gain per unit gain, maximum total net gain, amplification bit-rate, noise figure and amplification bandwidth.

In 2010, Bradley *et. al.* demonstrated a 5.4 cm long amplifier in erbium doped Al_2O_3 with a total internal peak net gain of 9.3 dB at a wavelength of 1533 nm for a launched pump power of almost 100 mW at 977 nm and a launched signal power of 1 µW [107]. An internal net gain of >3.5 dB was measured for the wavelength range of 1525–1565 nm. The erbium ion concentration in that device was 1.17×10^{20} cm^{-3}. The waveguide cross-section consisted of a ridge waveguide of thickness ~1 µm, width of 4 µm and measured ridge depth ranging between 50-99 nm. Such cross-section exhibited monomode behavior for both pump and signal wavelengths with ~80% overlap with the doped core and excellent overlap between the pump and signal modes. In a similar waveguide cross-section, Bradley *et. al.* demonstrated amplification of 170 Gbps signals [108]. An erbium concentration of 2.1×10^{20} cm^{-3} was utilized in the reported device. A peak net gain of ~11 dB was demonstrated for a launched pump power of 65 mW (at 1480 nm) and launched signals (1533 nm) ranging from 1 µW to 1 mW. Vázquez-Córdova *et. al.* reported a net peak internal gain of ~20 dB on spiral waveguide

amplifiers of lengths 12.9 cm and 24.4 cm and Er^{3+} concentrations of 1.92×10^{20} cm^{-3} and 0.95×10^{20} cm^{-3} respectively with incident pump power of 250 mW (i.e., estimated coupling efficiency to the waveguides ~10%) [109]. The waveguide cross-section utilized by Vázquez-Córdova *et. al.* was a shallowly etched waveguide of thickness 1 μm, width 1.5 μm and etch depth 0.35 μm. Very recently, Mu *et. al.* proposed a smaller waveguide cross-section (i.e., a channel waveguide of 1 μmx0.8 μm), with an erbium concentration of $1.7x10^{20}$ cm^{-3}. Such waveguide amplifier was integrated onto the Si_3N_4 integrated photonic platform via double-layer monolithic integration technology using adiabatic vertical tapers [78]. A net Si_3N_4- Si_3N_4 peak gain of 18 dB was achieved with a 10 cm long spiral amplifier at 1532 nm with a bidirectional pumping scheme with total incident pump power of 50 mW (estimated coupling losses ~12 dB for 976 nm wavelength) and incident signal power of -20 dBm [110].

The achievable gain depends on various parameters including the available pump power as well as the dopant concentration of rare-earth-ions that can be introduced into the material without clustering, which leads to luminescence quenching. To achieve high ion concentration, Rönn *et. al.* alternated monolayers of Al_2O_3 and Er_2O_3 at different ratios to control the average erbium concentration [27]. The layers were deposited with atomic layer deposition (Section 2.1) in the gap of Si_3N_4 slots waveguides with slot width of ~100 nm and strip size of ~460 × 460 nm^2. Using this technique, an erbium concentration of $4.1x10^{21}$ cm^{-3} was achieved. They demonstrated a maximum net gain of 1.98 dB for a 250 μm long amplifier with 4.5 mW launched pump power at 980 nm. Similar approach was utilized by Demirtas *et. al.* [74]. The researchers alternated 5 monolayers of Al_2O_3 and 5 monolayers of Er_2O_3 for a final thickness of ~0.72 μm with total erbium concentration of 1×10^{21} cm^{-3}. Channel waveguides had a trapezoidal cross-section with a base 3.95 μm wide and a top width of 2.36 μm. An internal net peak gain per unit length of 13.72 dB/cm was measured for a 2 mm long waveguide amplifier (i.e., 2.74 dB total internal net peak gain) when pumped at 980 nm with 30 mW of incident pump power.

Furthermore, optical amplification at 880 nm was demonstrated in a Nd^{3+} doped Al_2O_3 waveguide amplifier. A ridge waveguide cross-section of 3 μm thickness, 2.5 μm width and 1 μm etch depth and Nd^{3+} ion concentration of 0.5×10^{20} cm^{-3} delivered 2.42 dB of net internal gain for a launched pump power of 55 mW at 802 nm of wavelength [82].

5. On-chip lasers in Al_2O_3

The combination of low propagation losses and relatively high optical gain enables the use of rare-earth ion doped Al_2O_3 for the realization of on-chip lasers. Furthermore, the very small linewidth enhancement factor of rare-earth ion gain material, due to the lack of coupling between intensity and phase fluctuations leads to lasers with very narrow linewidths. In the following, we have classified the on-chip lasers developed in this material in two categories, namely lasers with cavities based on microring resonators and cavities based on distributed Bragg reflectors, both distributed feedback lasers (DFBs) and distributed Bragg reflector lasers (DBRs). An overview of the lasers reported in the literature with their performance parameters is given in Table 1.

5.1. Microring lasers on rare-earth ion doped Al_2O_3

From the development of the first layers with optical gain in rare-earth ion doped Al_2O_3, it still took over a decade before the first integrated laser in Er^{3+}:Al_2O_3 was demonstrated by Bradley *et.al.* [30]. The demonstrated laser cavity consisted of a ring resonator, where the pump and signal coupling was achieved using two consecutive directional couplers, as shown in Figure 8(a). The couplers were designed for high coupling of the pump into the cavity while keeping the coupling at the laser wavelength low to ensure a high-Q factor for the cavity. The output power versus launched pump power of this device is shown in Figure 8(b). Varying the coupler and cavity length the output

wavelength varied between 1530 and 1557 nm, showing the possibility for selecting the emission wavelength of the Er^{3+}:Al_2O_3 devices (Figure 8(c)). Due to the multi longitudinal mode nature of the ring cavity (i.e., cavity length ranging between 3 and 5.5 cm) and the used coupler design, the output was inherently multimode.

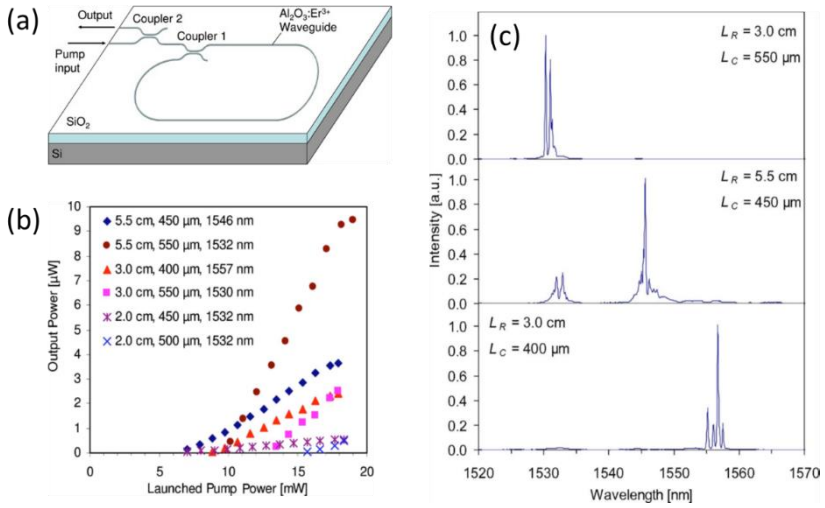

Figure 8. (a) Schematic of the laser cavity. (b) On-chip integrated laser output power vs. pump power launched into the chip for different resonator and output coupler lengths. The main lasing wavelength are indicated. (c) Laser output spectra for different coupler lengths LC and resonator lengths LR. (Figures taken from [30]).

Table 1 Overview of on-chip lasers on rare-earth ion doped Al_2O_3.

Reference	[83]	[3]	[81]	[13]	[30]	[44]	[22]	[31]	[40]	[41]	[34]	[35]	[10]	[37]	[38]	[77]	[36]	[36]	[45]	[8]	[21]	[33]	[41]	[97]	[45]	[39]
Year of publication	2019	2019	2019	2014	2010	2016	2012	2010	2013	2014	2016	2016	2017	2017	2017	2019	2017		2017	2018	2011	2013	2014	2020	2017	2018
Cavity type	Ring	Ring	ring	Ring	Ring	Ring	DFB	DFB	DFB	DFB	DFB	DFB	DFB	DFB	DFB	DFB	dps-DFB	qps-DFB	DFB	DFB	DBR	DBR	DBR	DBR	DBR	Vernier Ring
Rare earth Dopant	Yb	Yb	Er	Er / Yb	Er	Tm	Yb	Er	Er	Er	Er	Er	Er	Er	Er	Er	Er	Er	Tm	Ho	Yb	Er	Er	Er	Tm	Er
Doping concentration [10^{20} cm^{-3}]	--	--	--	2-3 / 7	1	2.5	5.8	3	1.7	1.3	0.9	1.5	1	1.2	1	1.5	1	1	3	3.2	5.8	1.4	1.3	1.5	3	1.5
Pump wavelength [nm]	976	976	976	976	980	1608	976	1480	975	974	1480	976	978	976	976	980	978, 976	978, 976	1612	1950	976	975, 978	974	980	1612	980
Laser wavelength [nm]	1030	1024	1532	1560 / 1042	1530-1557	1760-1920	1020	1545.2	1543	1560	1563	1563	1563-1580	1553	1592	1599	1565	1536, 1566, 1596	1861	2022-2101	1021	1536, 1561, 1596	1546	1564	1881	1524-1574
Minimal threshold pump power [mW]	12 (**)	7 (**)	--	0.5 / 0.7 (*)	6.4 (**)	0.773 (*)	5 (*)	15 (*)	81 (*)	21 (*)	31 (*)	~30 (*)	120 (*)	24.9 (*)	16 (*)	40 (*)	14 (*)	55 (*)	96 (*)	130 (*)	10 (*)	44 (*)	11 (*)	--	65 (*)	~30 (*)
Maximal slope efficiency [%]	1.2 (**)	0.1 (**)	--	0.3 / 8.4 (*)	0.11 (**)	24 (*)	41	6.2	0.006 (*)	0.77 (*)	7 (*)	2.2 (*)	--	1.3 (*)	0.7 (*)	0.01 (*)	2.9 (*)	0.6% (*)	14 (*)	2 (*)	6700%	2.6	5.2 (*)	0.02	23 (*)	2.2 (*)
Maximal laser output power [μW]	1.9×10^3 (**)	25 (**)	10 (**)	2.4 / 100 (*)	9.5 (**)	230 (*)	28×10^3 (**)	3×10^3 (**)	9 (*)	270 (*)	75×10^3 (*)	1×10^3 (*)	20 (*)	2.6×10^3 (*)	1.2×10^3 (*)	--	5.43×10^3 (*)	0.76×10^3 (*)	267×10^3 (*)	15×10^3 (*)	47×10^3 (**)	5.1×10^3 (*)	2.1×10^3 (*)	--	387×10^3 (*)	1.6×10^3 (*)
Linewidth [kHz]	--	250 (+)	--	--	--	--	4.5	1.7	501	--	--	--	--	--	--	--	5.3	30.4	--	--	--	--	--	--	--	340
Cavity length [mm]	3	0.63	1.8	1.0	20-55	0.628	10	10	7.5	21.5	23	20	5.5	15	20	20	20	20	20	20	10	20	20	20	20	46
Single longitudinal mode/multimode?	multi	single	single	single	multi	multi	single	single	single	single	single	single	single	single	single	single	single	single	single	single	single	--	single	--	single	single

(**) off chip, (*) on chip

(+) 50 ms integration time

A more compact design based on an Yb^{3+}:Al_2O_3 microdisk/microring coupled to a bus waveguide is reported in [3]. The radius of the microdisk is 100 μm and the bus waveguide has a width of 1.4 μm and an coupling gap of 0.6 μm. The thickness of the Al_2O_3 core is 0.55 μm. The bottom cladding is thermal SiO_2 8 μm thick and the top cladding is water or other liquid delivered through a PDMS microfluidics channel, such as urine (Figure 9). This device exhibited an output power of ~25 μW with a ~2% on-chip slope efficiency. Single-mode laser emission was obtained at a wavelength of 1024 nm with a linewidth of 250 kHz.

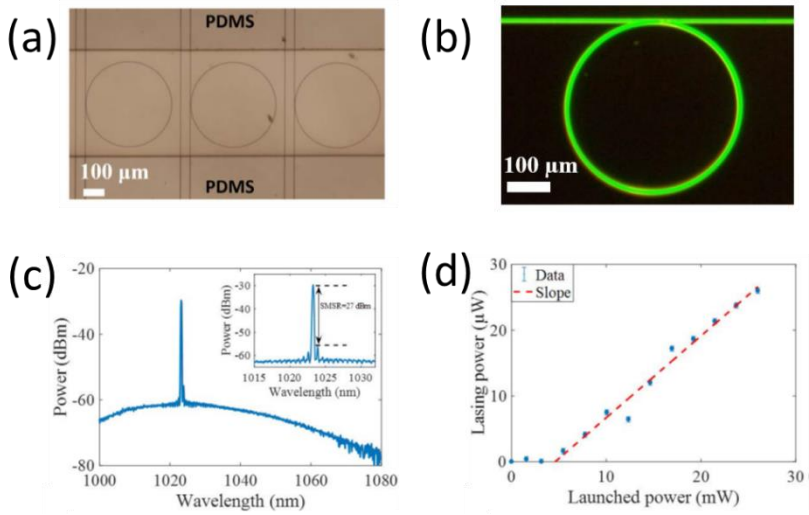

Figure 9. (a) Microring resonator inside a PDMS microfluidic channel. (b) Pump light coupled into a microdisk resonator. Green-light emission from excited Er^{3+} impurity. (c) Yb^{3+}:Al_2O_3 microdisk lasing spectrum. Inset shows zoom of the single-mode lasing peak. (d) On-chip integrated laser output power vs. pump power launched into the waveguide.

Unwanted absorption of the pump power and reabsorption of the lasing power outside the laser cavity can be reduced by integrating the doped Al_2O_3 onto a passive platform (Section 3). Bradley *et.al.* demonstrated a locally deposited rare-earth ion doped Al_2O_3 microring lasers connected to a SiN_x bus waveguide as shown in Figure 4 [12]. An output power of ~2.5 μW with double-side slope efficiency of 0.3% were measured. An on-chip laser output power of ~100 μW and double-side slope efficiency of 8.4% have been measured for an Yb^{3+}-doped microring laser coupled to a SiN_x bus waveguide [12]. Based on the same technology, Su *et.al.* demonstrated a thulium doped Al_2O_3 microring laser [44]. This laser exhibited an on-chip output power of ~220 μW and double-side slope efficiency of 24% with 1.6 μm resonant pumping and lasing in the wavelength range of 1.8-1.9 μm.

In order to optimize pump absorption in the microcavity while reducing coupling losses at the signal wavelength, which would increase the laser threshold, a wavelength division multiplexer (WDM) can be implemented. Such WDM permits tuning the coupling strength of the pump and laser wavelengths independently [83]. The design of the laser cavity is shown in Figure 10(a). This design was first demonstrated in Yb^{3+} doped Al_2O_3 for a biosensing application with a H_2O top cladding. A 2 mW multimode laser power was measured at the output fiber, corresponding to ~6 mW on-chip laser output power, which is the largest reported so far for a microring laser cavity in this material. A single side fiber-to-fiber slope efficiency of 1.2% has been measured, which corresponds to ~11% single side on-chip slope efficiency.

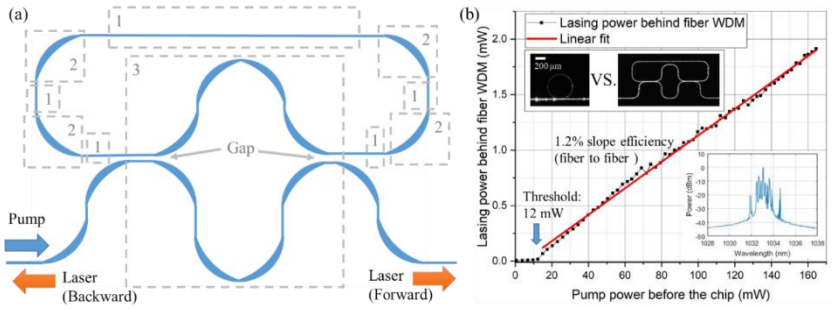

Figure 10. (a) Proposed micro ring laser cavity. Blue lines are the waveguides. The regions 1 (indicated with dashed gray boxes) are used for the design of the sensitivity (the waveguide width and thickness) and the free spectral range (length). The regions 2 are adiabatic bends, with negligible bending loss and straight to bend coupling loss. Region 3 is a Mach-Zehnder interferometer based WDM for independently selecting the coupling strength of the pumping and lasing wavelength. (b) Backward lasing power vs. pump power. The top insets are top view images of a typical ring laser and the proposed modular laser device operating with a H_2O cladding. The bottom inset is a typical multimode lasing spectrum of the proposed device. (Figures taken from [83])

The free spectral range (FSR) of a typical RE^{3+}:Al_2O_3 ring laser is much smaller than the gain bandwidth of the rare-earth ion. This, in general, leads to a multi-longitudinal mode behavior of these ring lasers. In order to achieve a single mode tunable laser, Li *et.al.* demonstrated a hybrid ring laser cavity with an Er^{3+}:Al_2O_3 waveguide as the gain section and two Si_3N_4 rings as intra-cavity tunable Vernier filter as shown in Figure 11 [39]. An on-chip laser output power of 1.6 mW and 2.2% on-chip slope efficiency were measured. The Si_3N_4 Vernier ring filters are thermally tuned resulting in a 46 nm wavelength tuning range.

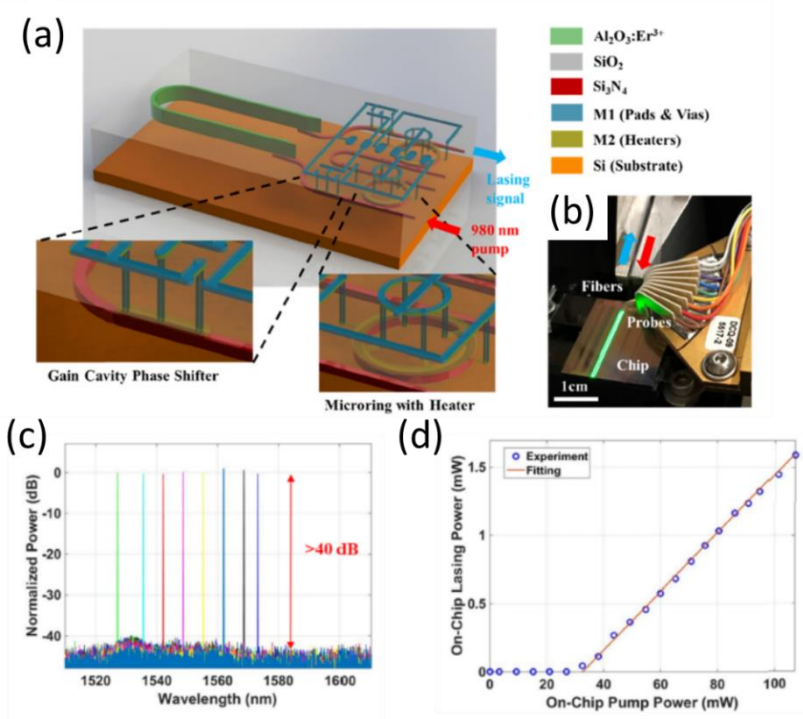

Figure 11. (a) 3D illustration of the external cavity laser design proposed in [39]. (b) Fabricated device on the test setup, showing the characteristic erbium green color upconversion with 980 nm pumping. (c) Laser output spectra showing 46 nm tuning range with >40 dB side mode suppression

ratio (SMSR). (d) On-chip laser output power with respect to launched on-chip pump power, showing a 2.2% slope efficiency. (Figures taken from [39])

5.2. DFB and DBR on-chip lasers in rare-earth ion doped Al_2O_3.

A single longitudinal mode operation laser in Er^{3+}:Al_2O_3 was first shown by Bernhardi *et. al.* [31] in a distributed feedback (DFB) waveguide cavity. The single frequency output with a linewidth of 1.7 kHz has, to the best of our knowledge, not yet been surpassed in Al_2O_3 based integrated lasers. The erbium doped waveguide, with a doping concentration of 3.0×10^{20} cm^{-3} and a length of 1 cm, was pumped at 1480 nm to obtain laser action with a threshold of 15 mW of launched pump power and 3 mW maximum off-chip output power with a slope efficiency of 6.2% with respect to launched pump power. The high slope efficiency is a consequence of the relatively strong mode confinement in the small cross section of the Er^{3+}:Al_2O_3 waveguide. The Er^{3+}:Al_2O_3 was deposited using a reactive sputter process, to produce a 1 μm thick layer onto which a 2.2 μm wide ridge was etched 100 nm deep using reactive ion etching.

Using the same material and waveguide geometry, a highly efficient monolithic distributed-Bragg-reflector laser doped with ytterbium was demonstrated. An ytterbium doping concentration of 5.8×10^{20} cm^{-3} and an effective cavity length of 4.13 mm was utilized. The lasers exhibited a threshold with respect to the launched pump power of 10 mW with a double side combined slope efficiency of 67% and a maximum combined double side off-chip output power of 47 mW [21]. By introducing a second phase shift region within the DFB laser cavity, a dual wavelength laser was demonstrated [22], which was used to produce a 9 kHz wide microwave signal at 15 GHz with a temporal stability of ±2.5 MHz.

As described in section 3, integration of rare-earth ion doped Al_2O_3 onto passive photonic platforms might pave the road to fully monolithically integrated photonic chips. In that direction, Purnawirman *et al.*[33] fabricated a distributed Bragg reflector (DBR) laser by combining a Si_3N_4 thin layer with a cladding in Al_2O_3 (Figure 5). A thin SiO_2 intermediate layer controlled the overlap between the mode and the active gain region. The laser cavity consisted of two sidewall corrugated distributed Bragg reflectors 2.5 mm long patterned on the sidewalls of the Si_3N_4 waveguide and a phase section of 20 mm of length. The erbium doping concentration was 1.4×10^{20} cm^{-3}. They showed an on-chip threshold pump power of 44 mW with an on-chip slope efficiency of 2.6% with a maximum on chip power of 5.1 mW. Wavelength selection was achieved by changing the grating period, with demonstrated lasing at 1536, 1561 and 1596 nm.

A similar design was reported by Belt *et. al.*, with the cross-section shown in Figure 12 [40]. A DFB cavity was fabricated with a sidewall corrugation grating. The authors fabricated an array of DFB cavities designed for different wavelengths, thereby creating a multiwavelength source with emission at 1531, 1534, 1537, 1540, and 1543 nm. The on-chip pump laser power threshold of the system was 81 mW and the internal slope efficiency was 5.7×10^{-3}%. This is likely a result of the short cavity length limiting the pump absorption. The low efficiency and therefore low output power resulted in a relatively broad linewidth of 501 kHz.

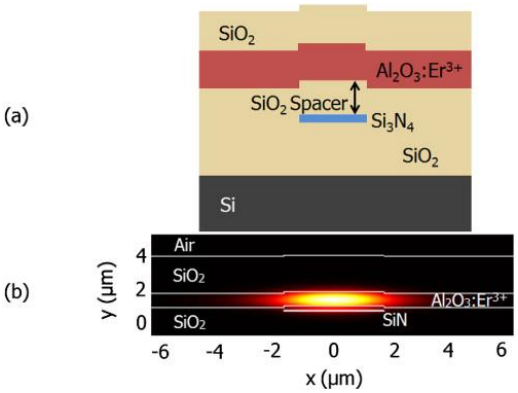

Figure 12 (a) Cross-section diagram of the Er^{3+}:Al_2O_3 lasing structure. (b) Simulated TE-mode profile for the lasing light at 1531 nm[40].

An improved pumping efficiency was demonstrated by Sing *et al.* [35]. They enclosed the DFB laser in a DBR cavity for the pump wavelength. When the cavity is pumped on resonance, the slope efficiency was improved by a factor of 1.8. In addition to resonance pumping, the waveguide cross-section was optimized to maximize overlap of both the pump and signal wavelength with the rare-earth ion doped Al_2O_3, thereby increasing the pump efficiency. The efficiency is further increased in this configuration by the increased overlap between the pump and signal mode. The waveguide architecture utilized consists of a multi stripe waveguide design, similar to the one proposed by Bradley *et al.*[12], which lowers the effective refractive index of the Si_3N_4 waveguide section, while maintaining significant thickness. A schematic of the resonant cavity as well as the waveguide cross-section is shown in Figure 13.

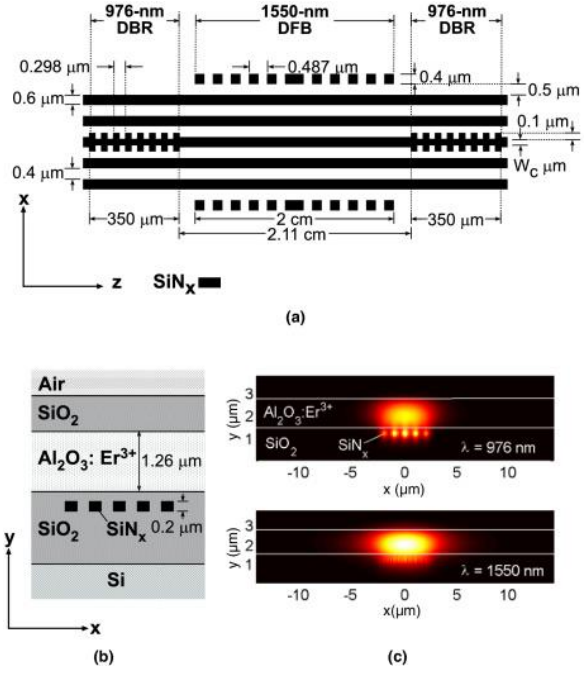

Figure 13. Design of the resonantly pumped DFB laser: (a) top view of the SiNx double-cavity structure showing 976 nm pump DBRs and the 1550 nm DFB. (b) Cross-sectional drawing of the composite waveguide structure. (c) Calculated intensity profiles of the 976 nm[35].

As discussed in Section 2, Magden *et al.* developed a fully CMOS compatible reactive sputtering deposition process of Al_2O_3 by reducing the temperature during deposition to 250 C. This was possible by applying a DC bias to the substrate to increase the kinetic energy of the aluminum and

erbium ions arriving to the substrate, therefore achieving similar morphology at a lower temperature [37]. The lower substrate temperature during deposition allows integration of the Al_2O_3 layers with active components in Si_3N_4, since the required metal contacts do not melt at this temperature. This technology is also compatible with integration on a CMOS platform. The achieved on-chip pump threshold and slope efficiency of a quarter wave shift DFB cavity for a doping concentration of 1.9×10^{20} cm^{-3} were 24.9 mW and 1.3% respectively, for an emission wavelength of 1553 nm. An on-chip laser output of 2.6 mW at 1552.98 nm was obtained for an on-chip pump power of 220 mW at 976 nm of wavelength.

Another improvement in the design of DFB laser cavities is introduced by Purnawirman *et al.*[38] where a curvature is added to the waveguides comprising the DFB cavity to compensate for the non-uniformity in the active Al_2O_3 layer thickness. Using this technique, a 6-fold reduction in the on-chip threshold power (i.e., 16 mW) is reported with respect to the control straight waveguide DFB laser (i.e., 105 mW). An on-chip laser power of 1.2 mW was demonstrated with this architecture.

Despite the many improvements on the initial DFB lasers integrated with Si_3N_4, the threshold power, slope efficiency and linewidth of the DFB laser by Bernhardi *et al.*[31] have not yet been achieved by a quarter phase shifted (QPS) cavity design (Figure 13). An alternative phase shift approach is proposed and demonstrated by Purnawirman *et al.* [36]. The quarter phase shift is now generated by tapering the thickness of one of the waveguide ridges segments. The distributed phase shift (DPS) element approach is similar to the varying waveguide width proposed in the DFB laser by Bernhardi *et al.*[31], also resulting in very similar behavior. The structure of the laser as well as its performance are shown in Figure 14. The achieved on-chip pump threshold was 14 mW with a slope efficiency of 2.9% and maximal on-chip output power of 5.4 mW. The linewidth of the DPS-DFB laser was measured to be 5.3 kHz, showing an almost 6-fold improvement compared to the QPS-DFB laser [36].

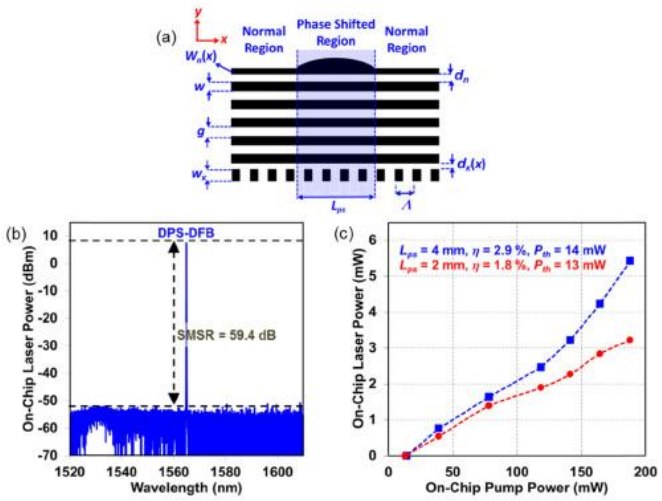

Figure 14 (a) Design of Er^{3+}:Al_2O_3 DPS-DFB laser with a five-segment SiN_x waveguide (not to scale). The cavity structure consists of five continuous SiN_x segments with grating perturbation provided by two additional side pieces, one with a phase shift region (top); (b) Spectrum of the proposed laser; (c) On-chip laser output power as a function of on-chip pump power [36].

6. Applications of RE^{3+}:Al_2O_3 on-chip lasers on a passive photonic platform

Passive ring resonators are popular for sensing applications due to their high-Q and high sensitivity to environmental changes [111-115]. A lasing ring cavity has a much higher Q than its cold cavity, which leads to a lower intrinsic limit of detection of the sensor [116,117].

An Yb^{3+}:Al_2O_3 microdisk laser has been recently demonstrated for the label-free detection of cancer biomarkers directly from undiluted urine [3]. The top cladding of this laser is the liquid to be sensed, in this case urine, which is delivered through a microfluidic channel. Attachment of the biomolecules onto the Yb^{3+}:Al_2O_3 waveguide leads to a change of the effective refractive index, which subsequently changes the optical path length of the laser cavity and therefore the lasing frequency. The frequency shift is accurately detected by heterodyning the output of the microdisk laser with that of an external reference laser. This type of sensor is not only sensitive to biomolecules binding on the surface of the waveguide but it is also sensitive to temperature and bulk refractive index changes. These sensitivities have been characterized (Figure 15) to be 1.7 GHz/K (6 pm/K) and 5.7 THz/RIU (20 nm/RIU). A limit-of-detection of 300 pM (3.6 ng/ml) of the protein rhS100A4 (12 kDa) in urine was experimentally demonstrated, being mostly limited by thermal noise. This result shows the potential of integrated active microdisk lasers in Al_2O_3 for biosensing.

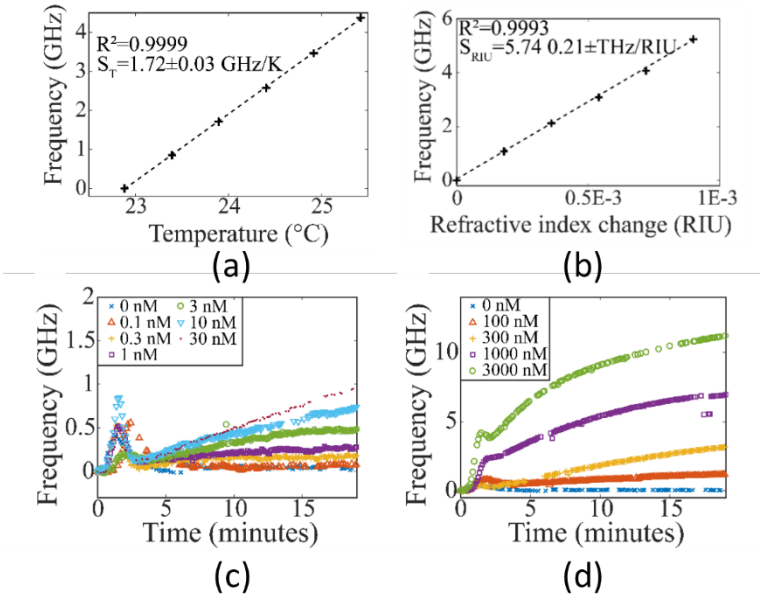

Figure 15. (a) Temperature slope sensitivity. The dotted line is a linear fit. (b) Bulk refractive index slope sensitivity. The dotted line is a linear fit. (c) Beatnote frequency changes due to binding of the rhS100A4 protein to the antibodies immobilized onto the microdisk laser at low protein concentrations. The initial bumps at ~1—2 minutes are results of a short-time temperature overshoot caused by the dynamics of the flow system. (d) Data of high protein concentrations. (Figures taken from [3]).

Benefiting from all the developments discussed above in this review paper, namely the development of low-loss Al_2O_3 deposited at low temperature [37], integration with Si_3N_4 using a trench configuration [12, 39, 44], DFB laser design [35, 36, 118] and adiabatic transitions from the hybrid active gain region to the passive Si_3N_4 waveguides [39, 78-79], complex systems can be built. An impressive demonstration of such system for LIDAR application was recently presented by Notaros *et. al.* [77]. A first proof-of-concept of an electrically steerable integrated phased array activated by an on-chip erbium doped DFB laser was demonstrated (Figure 16). A steering angle of 0.85°x0.20° as well as 30°/W electrical steering efficiency were experimentally shown.

A silicon photonics data link integrating an Er^{3+}:Al_2O_3- Si_3N_4 DBR laser similar to the one reported in [35] with a silicon photonics circuit integrating modulators and germanium photodetectors has also

been recently demonstrated [97]. These demonstrations show the potential of this material for real-life applications.

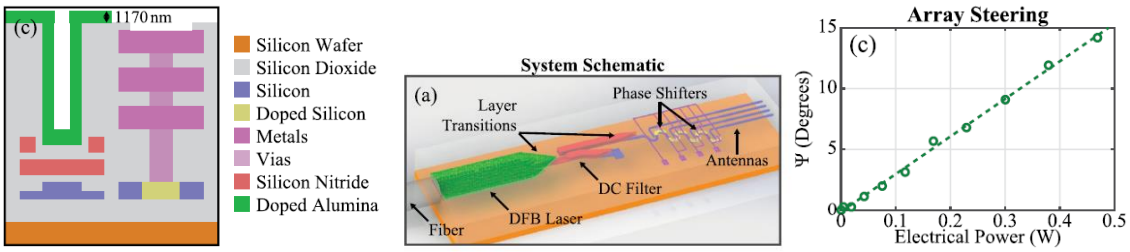

Figure 16. (a) Integration of Er^{3+}:Al_2O_3 with Si_3N_4 waveguide integrated onto a CMOS process. (b) Schematic of the whole device including the optically pumped DFB laser, a filter and the phase arrayed antennas. (c) Steering of the array as a function of applied electrical power. Figure taken from [77].

7. Final remark

Rare-earth ion doped Al_2O_3 is an active optical material that has gained growing interest in recent years owed to the excellent optical properties of the host, Al_2O_3, in combination with the gain performance provided by the rare-earth ions. Recent developed monolithic integration technologies of this material onto the passive silicon on insulator and silicon nitride technologies permits the development of complex circuits, where the properties of the on-chip generated light can be controlled by the passive circuitry. This technology opens the road to potentially disruptive devices that can find interesting applications in emerging fields including LiDAR, quantum technology, optical sensing/metrology and artificial intelligence.

Funding: This project has received funding from the European Research Council (ERC) under the European Union's Horizon 2020 research and innovation program (grant agreement n° 648978) and European Union's Horizon 2020 Framework Program under grant agreement No 634928 (GLAM). The results presented here reflect only the views of the authors; the European Commission is not responsible for any use that may be made of the information it contains.

References

1. E. R. Dobrovinskaya, L. A. Lytvynov, and V. Pishchik, Sapphire Material, Manufacturing, Applications (Springer, 2009).
2. G. N. West, W. Loh, D. Kharas, C. Sorace-Agaskar, K. K. Mehta, J. Sage, J. Chiaverini, and R. J. Ram, "Low-loss integrated photonics for the blue and ultraviolet regime," APL Photonics 4(2), 026101 (2019).
3. M. de Goede, L. Chang, J. Mu, M. Dijkstra, R. Obregón, E. Martínez, L. Padilla, F. Mitjans, and S. M. Garcia-Blanco, "Al_2O_3: Yb^{3+} integrated microdisk laser label-free biosensor," Opt. Lett. 44, 5937-5940 (2019).
4. M. de Goede, M. Dijkstra, R. Obregón, J. Ramón-Azcón, E. Martínez, L. Padilla, F. Mitjans, and S. M. Garcia-Blanco, " Al_2O_3 microring resonators for the detection of a cancer biomarker in undiluted urine," Opt. Express 27(13), 18508 (2019).
5. E. H. Bernhardi, Q. Lu, H. A. G. M. Van Wolferen, K. Wörhoff, R. M. De Ridder, and M. Pollnau, "Monolithic distributed Bragg reflector cavities in Al_2O_3 with quality factors exceeding 10^6," Photonics Nanostructures - Fundam. Appl. 9(3), 225–234 (2011).
6. J. D. B. Bradley, F. Ay, K. Wörhoff, and M. Pollnau, "Fabrication of low-loss channel waveguides in Al_2O_3 and Y2O3 layers by inductively coupled plasma reactive ion etching," Appl. Phys. B 89(2–3), 311–318 (2007).
7. S. A. Vázquez-Córdova, M. Dijkstra, E. H. Bernhardi, F. Ay, K. Wörhoff, J. L. Herek, S. M. García-Blanco, and M. Pollnau, "Erbium-doped spiral amplifiers with 20 dB of net gain on silicon," Opt. Express 22(21), 25993 (2014).

8. N. Li, E. S. Magden, Z. Su, N. Singh, A. Ruocco, M. Xin, M. Byrd, P. T. Callahan, J. D. B. Bradley, C. Baiocco, D. Vermeulen, and M. R. Watts, "Broadband 2-μm emission on silicon chips: monolithically integrated Holmium lasers," Opt. Express 26(3), 2220 (2018).
9. K. Worhoff, J. D. B. Bradley, F. Ay, D. Geskus, T. P. Blauwendraat, and M. Pollnau, "Reliable Low-Cost Fabrication of Low-Loss Al_2O_3: Er^{3+} Waveguides With 5.4-dB Optical Gain," IEEE J. Quantum Electron. 45(5–6), 454–461 (2009).
10. Purnawirman, Nanxi Li, E. Salih Magden, Gurpreet Singh, Michele Moresco, Thomas N. Adam, Gerard Leake, Douglas Coolbaugh, Jonathan D. B. Bradley, and Michael R. Watts, "Wavelength division multiplexed light source monolithically integrated on a silicon photonics platform," Opt. Lett. 42, 1772-1775 (2017).
11. M. Demirtas, C. Odaci, N. K. Perkgoz, C. Sevik, and F. Ay, "Low Loss Atomic Layer Deposited Al_2O_3 Waveguides for Applications in On-Chip Optical Amplifiers," IEEE J. Sel. Top. Quantum Electron. 24(4), 1–8 (2018).
12. W.A.P.M. Hendriks, et. al., "Low loss aluminium oxide with high refractive index," Proc. ECIO (2020).
13. J. D. B. Bradley, E. S. Hosseini, Z. Su, T. N. Adam, G. Leake, D. Coolbaugh, and M. R. Watts, "Monolithic erbium- and ytterbium-doped microring lasers on silicon chips," Opt. Express 22(10), 12226–12237 (2014).
14. Z. Su, N. Li, H. C. Frankis, E. S. Magden, T. N. Adam, G. Leake, D. Coolbaugh, J. D. B. Bradley, M. R. Watts, "High-Q-factor Al_2O_3 micro-trench cavities integrated with silicon nitride waveguides on silicon," Opt. Express 26, 11161-11170 (2018)
15. J. D. B. Bradley and M. Pollnau, "Erbium-doped integrated waveguide amplifiers and lasers," Laser Photon. Rev. 5(3), 368–403 (2011).
16. P. G. Kik and A. Polman, "Erbium-Doped Optical-Waveguide Amplifiers on Silicon," MRS Bull. 23(04), 48–54 (1998).
17. Eric Lallier, "Rare-earth-doped glass and LiNbO3 waveguide lasers and optical amplifiers," Appl. Opt. 31, 5276-5282 (1992).
18. S. Blaize, L. Bastard, C. Cassagnètes, and J. E. Broquin, "Multiwavelengths DFB Waveguide Laser Arrays in Yb–Er Codoped Phosphate Glass Substrate," IEEE Photonics Technol. Lett 15, 516-518 (2003).
19. L. Bastard, S. Blaize, and J. E. Broquin, "Glass integrated optics ultranarrow linewidth distributed feedback laser matrix for dense wavelength division multiplexing applications," Opt. Eng. 42(10), 2800–2804 (2003).
20. J. Yang, K. van Dalfsen, K. Wörhoff, F. Ay, and M. Pollnau, "High-gain Al_2O_3:Nd^{3+} channel waveguide amplifiers at 880 nm, 1060 nm, and 1330 nm," Appl. Phys. B 101(1–2), 119–127 (2010).
21. E. H. Bernhardi, H. A. G. M. Van Wolferen, K. Wörhoff, R. M. De Ridder, and M. Pollnau, "Highly efficient, low-threshold monolithic distributed-Bragg-reflector channel waveguide laser in Al_2O_3:Yb^{3+}," Opt. Lett. 36(5), 603–605 (2011).
22. E. H. Bernhardi, M. R. H. Khan, C. G. H. Roeloffzen, H. a. G. M. van Wolferen, K. Wörhoff, R. M. de Ridder, and M. Pollnau, "Photonic generation of stable microwave signals from a dual-wavelength Al_2O_3:Yb^{3+} distributed-feedback waveguide laser," Opt. Lett. 37(2), 181 (2012).
23. G. N. van den Hoven, E. Snoeks, A. Polman, J. W. M. van Uffelen, Y. S. Oei, and M. K. Smit, "Photoluminescence characterization of Er-implanted Al_2O_3 films," Appl. Phys. Lett. 62(24), 3065–3067 (1993).
24. G. N. van den Hoven, J. A. van der Elsken, A. Polman, C. van Dam, K. W. M. van Uffelen, and M. K. Smit, "Absorption and emission cross sections of Er^{3+} in Al_2O_3 waveguides," Appl. Opt. 36(15), 3338–3441 (1997).
25. G. N. Van Den Hoven, R. J. I. M. Koper, A. Polman, C. Van Dam, J. W. M. Van Uffelen, and M. K. Smit, "Net optical gain at 1.53 μm in Er-doped Al_2O_3 waveguides on silicon," Appl. Phys. Lett., vol. 68, no. 14, pp. 1886–1888, Apr. 1996.
26. S. Musa, H. J. van Weerden, T. H. Yau, and P. V. Lambeck, "Characteristics of Er-doped Al_2O_3 thin films deposited by reactive co-sputtering," IEEE J. Quantum Electron. 36(9), 1089–1097 (2000).
27. J. Rönn, W. Zhang, A. Autere, X. Leroux, L. Pakarinen, C. Alonso-Ramos, A. Säynätjoki, H. Lipsanen, L. Vivien, E. Cassan, and Z. Sun, "Ultra-high on-chip optical gain in erbium-based hybrid slot waveguides," Nat. Commun. 10, 432 (2019).
28. -M Demırtaş, C Odaci, NK Perkgöz, C Sevık, F Ay, "Control of optical amplification process with extremely low background loss in Er: Al_2O_3Waveguides", 2017 IEEE Photonics Conference (IPC), 561-562, (2017).

29. J. D. B. Bradley, R. Stoffer, A. Bakker, L. Agazzi, F. Ay, K. Worhoff, and M. Pollnau, "Integrated Al_2O_3:Er^{3+} Zero-Loss Optical Amplifier and Power Splitter With 40-nm Bandwidth," IEEE Photonics Technol. Lett. 22, 278–280 (2010).
30. J. D. Bradley, R. Stoffer, L. Agazzi, F. Ay, K. Wörhoff, and M. Pollnau, "Integrated Al_2O_3: Er^{3+} ring lasers on silicon with wide wavelength selectivity," Opt. Lett. 35(1), 73–75 (2010).
31. E. H. Bernhardi, H. A. G. M. van Wolferen, L. Agazzi, M. R. H. Khan, C. G. H. Roeloffzen, K. Wörhoff, M. Pollnau, and R. M. de Ridder, "Ultra-narrow-linewidth, single-frequency distributed feedback waveguide laser in Al_2O_3: Er^{3+} on silicon," Opt. Lett. 35(14), 2394–2396 (2010).
32. M. Pollnau, "Rare-Earth-Ion-Doped Channel Waveguide Lasers on Silicon," 21(1), (2015).
33. Purnawirman, J. Sun, T. N. Adam, G. Leake, D. Coolbaugh, J. D. B. Bradley, E. Shah Hosseini, and M. R. Watts, "C- and L-band erbium-doped waveguide lasers with wafer-scale silicon nitride cavities," Opt. Lett. 38, 1760-1762 (2013).
34. E. S. Hosseini, J. D. B. Bradley, J. Sun, G. Leake, T. N. Adam, D. D. Coolbaugh, and M. R. Watts, "CMOS-compatible 75 mW erbium-doped distributed feedback laser," Opt. Lett. 39(11), 3106 (2014).
35. G. Singh, Purnawirman, J. D. B. Bradley, N. Li, E. S. Magden, M. Moresco, T. N. Adam, G. Leake, D. Coolbaugh, and M. R. Watts, "Resonant pumped erbium-doped waveguide lasers using distributed Bragg reflector cavities," Opt. Lett. 41, 1189-1192 (2016).
36. Purnawirman, N. Li, E. S. Magden, G. Singh, N. Singh, A. Baldycheva, E. S. Hosseini, J. Sun, M. Moresco, T. N. Adam, G. Leake, D. Coolbaugh, J. D. B. Bradley, and M. R. Watts, "Ultra-narrow-linewidth Al_2O_3: Er^{3+} lasers with a wavelength-insensitive waveguide design on a wafer-scale silicon nitride platform," Opt. Express 25(12), 13705 (2017).
37. E. Salih Magden, N. Li, Purnawirman, J. D. B. Bradley, N. Singh, A. Ruocco, G. S. Petrich, G. Leake, D. D. Coolbaugh, E. P. Ippen, M. R. Watts, and L. A. Kolodziejski, "Monolithically-integrated distributed feedback laser compatible with CMOS processing," Opt. Express 25, 18058-18065 (2017).
38. Purnawirman, N. Li, G. Singh, E. S. Magden, Z. Su, N. Singh, M. Moresco, G. Leake, J. D. B. Bradley, and M. R. Watts, "Reliable integrated photonic light sources using curved Al_2O_3: Er^{3+} distributed feedback lasers," IEEE Photonics J. 9, 1–9 (2017).
39. N. Li, D. Vermeulen, Z. Su, E. S. Magden, M. Xin, N. Singh, A. Ruocco, J. Notaros, C. V. Poulton, E. Timurdogan, C. Baiocco, and M. R. Watts, "Monolithically integrated erbium-doped tunable laser on a CMOS-compatible silicon photonics platform," Opt. Express 26(13), 16200 (2018).
40. M. Belt, T. Huffman, M. L. Davenport, W. Li, J. S. Barton, and D. J. Blumenthal, "Arrayed narrow linewidth erbium-doped waveguide-distributed feedback lasers on an ultra-low-loss silicon-nitride platform," Opt. Lett. 38(22), 4825 (2013).
41. M. Belt and D. J. Blumenthal, "Erbium-doped waveguide DBR and DFB laser arrays integrated within an ultra-low-loss Si_3N_4 platform," Opt. Express 22(9), 10655 (2014).
42. P. Pintus, S. Faralli, and F. Di Pasquale, "Integrated 2.8 μm laser source in Al_2O_3: Er^{3+} slot waveguide on SOI," J. Lightwave Technol. 29, 1206-1212 (2011).
43. J. Rönn, L. Karvonen, C. Kauppinen, A. P. Perros, N. Peyghambarian, H. Lipsanen, A. Säynätjoki, and Z. Sun, "Atomic Layer Engineering of Er-Ion Distribution in Highly Doped Er: Al_2O_3 for Photoluminescence Enhancement," ACS Photonics 3, 2040–2048 (2016).
44. Z. Su, N. Li, E. Salih Magden, M. Byrd, Purnawirman, T. N. Adam, G. Leake, D. Coolbaugh, J. D. B. Bradley, and M. R. Watts, "Ultra-compact and low-threshold thulium microcavity laser monolithically integrated on silicon," Opt. Lett. 41(24), 5708 (2016).
45. N. Li, Purnawirman, Z. Su, E. Salih Magden, P. T. Callahan, K. Shtyrkova, M. Xin, A. Ruocco, C. Baiocco, E. P. Ippen, F. X. Kärtner, J. D. B. Bradley, D. Vermeulen, and M. R. Watts, "High-power thulium lasers on a silicon photonics platform," Opt. Lett. 42(6), 1181 (2017).
46. M. K. Smit, G. A. Acket, and C. J. van der Laan, "Al_2O_3 films for integrated optics," Thin Solid Films 138(2), 171–181 (1986).
47. C. I. Emmerik, M. Dijkstra, M. de Goede, L. Chang, J. Mu, and S. M. García-Blanco, "Single-layer active-passive Al_2O_3 photonic integration platform," Opt. Mater. Express 8(10), 3049–3054 (2018).

48. L. Agazzi, J. D. B. Bradley, M. Dijkstra, F. Ay, G. Roelkens, R. Baets, K. Wörhoff, and M. Pollnau, "Monolithic integration of erbium-doped amplifiers with silicon-on-insulator waveguides," Opt. Express 18(26), 27703 (2010).
49. P. F. Jarschel, M. C. M. M. Souza, R. B. Merlo, N. C. Frateschi. “Loss compensation in microring-based Si photonics devices via Er^{3+} doped claddings,” IEEE Photon J 10, 1–12 (2018).
50. P.F. Jarschel, N.C. Frateschi, “Resonant amplification via Er-doped clad Si photonic molecules: Towards compact low-loss/high-Q Si photonic devices,” Solid State Electronics 155, 144–149 (2019).
51. M. Theurer , M. Moehrle, A. Sigmund, K.-O. Velthaus, R. M. Oldenbeuving, L. Wevers, F. M. Postma, R. Mateman, F. Schreuder, D. Geskus, K. Wörhoff, R. Dekker, R. G. Heideman, and M. Schell, “Flip-Chip Integration of InP and SiN,” IEEE Photon. Technol. Lett. 31, 273-276 (2019).
52. T. Ishizaka and Y. Kurokawa, "Optical properties of rare-earth ion (Gd^{3+}, Ho^{3+}, Pr^{3+}, Sm^{3+}, Dy^{3+} and Tm^{3+}) -doped alumina films prepared by the sol–gel method," J. Lumin. 92, 57–63 (2000).
53. A. Pillonnet-Minardi, O. Marty, C. Bovier, C. Garapon, J. Mugnier, “Optical and structural analysis of Eu3+-doped alumina planar waveguides elaborated by the sol-gel process,” Opt. Mater. 16, 9-13 (2001).
54. T. Ishizaka, R. Nozaki, and Y. Kurokawa, "Luminescence properties of Tb^{3+} and Eu^{3+}-doped alumina films prepared by sol-gel method under various conditions and sensitized luminescence," J. Phys. Chem. Solids 63, 613–617 (2002).
55. X. J. Wang, M. K. Lei, “Preparation and photoluminescence of Er^{3+}-doped Al_2O_3 films by sol-gel method,” Thin Solid Films 476, 41-45 (2005).
56. Z. H. Zhu, M. J. Sha, M. K. Lei, “Controllable formation of Er^{3+}- Yb^{3+} codoped Al_2O_3 films by the non-aqueous sol-gel method,” Thin Solid films 516, 5075-5078 (2008).
57. B. Hu, M. Yao, R. Xiao, J. Chen, X. Yao, “Optical properties of amorphous Al_2O_3 thin films prepared by a sol-gel process,” Ceram. Int. 40, 14133-14139 (2014).
58. W. Koh, S.-J. Ku, Y. Kim, “Chemical vapor deposition of Al_2O_3 films using highly volatile single sources,” Thin Solid Films 304, 222-234 (1997).
59. J. L. Deschanvres, W. Meffre, J. C. Joubert, J. P. Senateur, F. Robaut, J. E. Broquin, R. Rimet, “Rare-earth doped alumina thin films deposited by liquid source CVD processes,” J. Alloy. Compd. 275-277, 742-745 (1998).
60. M. Jiménez de Castro, R. Serna, J. A. Chaos, C. N. Afonso, E. R. Hodgson, “Influence of defects on the photoluminescence of pulsed-laser deposited Er-doped amorphous Al_2O_3 films,” Nucl. Instrum. Method. B 166-167, 793-797 (2000).
61. R. Serna, M. Jiménez de Castro, J. A. Chaos, A. Suárez-Garcia, C. N. Afonso, M. Fernández, and I. Vickridge, “Photoluminescence performance of pulsed laser deposited thin films with large erbium concentrations,” J. Appl. Phys. 90, 5120 (2001).
62. A. Suárez-García, J. Gonzalo, C. N. Afonso, “Low-loss Al_2O_3 waveguides produced by pulsed laser deposition at room temperature,” Appl. Phys. A 77, 779-783 (2003).
63. R. Serna, A. Suárez-Garcia, M. Jiménez de Castro, C. N. Afonso, “Improving the photoluminescence of thin films by nanostructuring the rare-earth ion distribution,” Appl. Surf. Sci. 247, 8-17 (2005).
64. M. Jiménez de Castro, A. Suárez-García, R. Serna, C. N. Afonso, J. García-López, “Optical activation of Er^{3+} in Al_2O_3 during pulsed laser deposition,” Opt. Mater. 29, 539-542 (2007).
65. R. Serna, S. Nunez-Sanchez, F. Xu, C. N. Afonso, “Enhanced photoluminescence of rare-earth doped films prepared by off-axis pulsed laser deposition,” Appl. Surf. Sci. 257, 5204-5207 (2011).
66. M. M. Aslan, N. A. Webster, C. L. Byard, M. B. Pereira, C. M. Hayes, R. S. Wiederkehr, and S. B. Mendes, "Low-loss optical waveguides for the near ultra-violet and visible spectral regions with Al_2O_3 thin films from atomic layer deposition.," Thin Solid Films 518, 4935–4940 (2010).
67. A. Wickberg, C. Keininger, C. Sürgers, S. Schlabach, X. Mu, C. Koos, M. Wegener, “Second harmonic generation from ZnO/ Al_2O_3 nanolaminate optical metamaterials grown by atomic-layer deposition,” Adv. Optical Mater. 4, 1203-1208 (2016).

68. M. Demirtas, C. Odaci, N. K. Perkgoz, C. Sevik, and F. Ay, “Low loss atomic layer deposited Al_2O_3 waveguides for applications in on-chip optical amplifiers,” IEEE J. Sel. Top. Quantum Electron. 24, 1–8 (2018).
69. R. L. Puurunen, “Surface chemistry of atomic layer deposition: a case study for the trimethylaluminum/water process,” J. Appl. Phys. 97, 121301 (2005).
70. S. M. George, "Atomic Layer Deposition: An Overview," Chem. Rev. 110, 111–131 (2010).
71. J. López, H. A. Borbón-Nuñez, E. G. Lizarraga-Medina, E. Murillo, R. Machorro, N. Nedev, H. Marquez, M. H. Farías, H. Tiznado, and G. Soto, " Al_2O_3-Y_2O_3 ultrathin multilayer stacks grown by atomic layer deposition as perspective for optical waveguides applications," Opt. Mater. 72, 788–794 (2017).
72. -M Demirtaş, A Özden, E Açikbaş, F Ay, “Extensive mode mapping and novel polarization filter design for ALD grown Al_2O_3 ridge waveguides”, Opt. Quantum Electron. 48 (7), 357, (2016).
73. -A Özden, M Demirtaş, F Ay, “Polarization insensitive single mode Al_2O_3 rib waveguide design for applications in active and passive optical waveguides”, J. Eur. Opt. Soc.-Rapid Publ. 10, 15005, (2015).
74. M. Demirtaş and F. Ay, "High-gain Er^{3+}: Al_2O_3 on-chip waveguide amplifiers," IEEE J. Selec. Top. Quant. Electron. 26, 1-8 (2020).
75. K. Worhoff, F. Ay, and M. Pollnau, "Optimization of low-loss Al_2O_3 waveguide fabrication for application in active integrated optical devices," ECS Trans. 3, 17–26 (2006).
76. C. I. van Emmerik, et. al., "Relative oxidation state of the target as guideline for depositing optical quality RF reactive magnetron sputtered Al_2O_3 layers," Opt. Mater. Express 10, 1451-1462 (2020).
77. J. Notaros, N. Li, C. V. Poulton, Z. Su, M. J. Byrd, E. S. Magden, E. Timurdogan, C. Baiocco, N. M. Fahrenkopf, and M. R. Watts, "CMOS-compatible optical phased array powered by a monolithically-integrated erbium laser," J. Lightwave Technol. 37, 5982-5987 (2019).
78. J. Mu, M. Dijkstra, Y.-S. Yong, M. de Goede, L. Chang, S. M. García-Blanco, "Monolithic integration of Al_2O_3 and Si_3N_4 toward double-layer active-passive platform, " IEEE J. Selec. Top. Quant. Electron. 25, 8200911 (2019).
79. J. Mu, M. Dijkstra, S. M. García-Blanco, "Resonant coupling for active-passive monolithic integration of Al_2O_3 and Si_3N_4," IEEE Photonics Technol. Lett. 31, 771 - 774 (2019).
80. J. Mu, M. Dijkstra, and S. M. García-Blanco, "Monolithic integration of Al_2O_3: Er^{3+} amplifiers in Si_3N_4 technology," in 2019 Conference on Lasers and Electro-Optics Europe and European Quantum Electronics Conference, OSA Technical Digest (Optical Society of America, 2019), paper ca_p_38.
81. J. Mu, M. Dijkstra, and S. M. García-Blanco, “Monolithically integrated microring lasers in silicon nitride photonics,” in Proc. Annual Symp. IEEE Benelux Photonics Society, Amsterdam (2019).
82. J. Yang et al., "Integrated optical backplane amplifier," IEEE J. Selec. Top. Quant. Electron. 17, 609-616 (2011).
83. L. Chang, M. de Goede, M. Dijkstra, C. I. van Emmerik, and S. M. García-Blanco, "Performance parameter decoupled high efficiency micro ring laser cavity for biosensing," in 2019 Conference on Lasers and Electro-Optics Europe and European Quantum Electronics Conference, OSA Technical Digest (Optical Society of America, 2019), ch_5_4.
84. Purnawirman, N. Li, G. Singh, E. S. Magden, Z. Su, N. Singh, M. Moresco, G. Leake, J. D. B. Bradley, and M. R. Watts, “Reliable integrated photonic light sources using curved Al_2O_3 Er^{3+} distributed feedback lasers,” IEEE Photonics J. 9, 1–9 (2017).
85. Purnawirman, N. Li, E. S. Magden, G. Singh, N. Singh, A. Baldycheva, E. S. Hosseini, J. Sun, M. Moresco, T. N. Adam, G. Leake, D. Coolbaugh, J. D. B. Bradley, and M. R. Watts, "Ultra-narrow-linewidth Al_2O_3: Er^{3+} lasers with a wavelength-insensitive waveguide design on a wafer-scale silicon nitride platform," Opt. Express 25, 13705-13713 (2017).
86. Artur Hermans, Michiel Van Daele, Jolien Dendooven, Stéphane Clemmen, Christophe Detavernier, and Roel Baets, "Integrated silicon nitride electro-optic modulators with atomic layer deposited overlays," Opt. Lett. 44, 1112-1115 (2019).
87. A. Wickberg, C. Kieninger, C. Sürgers, S. Schlabach, X. Mu, C. Koos, and M. Wegener, “Second-harmonic generation from ZnO/ Al_2O_3 nanolaminate optical metamaterials grown by atomic-layer deposition,” Adv. Opt. Mater. 4, 1203 (2016).

88. S. Berg, T. Nyberg, “Fundamental understanding and modeling of reactive sputtering processes,” Thin Solid Films 476, 215– 230 (2005).

89. D. Depla, S. Mahieu, R. De Gryse, “Magnetron sputter deposition: Linking discharge voltage with target properties,” Thin Solid Films 517, 2825–2839 (2009).

90. S. Mahieu, P. Ghekiere, D. Depla, and R. De Gryse, "Biaxial alignment in sputter deposited thin films," Thin Solid Films 515, 1229–1249 (2006).

91. K. Bobzin, E. Lugscheider, M. Maes, C. Pinero, “Relation of hardness and oxygen flow of Al_2O_3 coatings deposited by reactive bipolar pulsed magnetron sputtering,” Thin Solid Films 494, 255 – 262 (2006).

92. K. Strijckmans, R. Schelfhout, and D. Depla, “Tutorial: Hysteresis during the reactive magnetron sputtering process,” J. Appl. Phys. 124, 241101 (2018).

93. P. Loiko, N. Ismail, J. D. B. Bradley, M. Götelid, and M. Pollnau, "Refractive-index variation with rare-earth incorporation in amorphous Al_2O_3 thin films," J. Non. Cryst. Solids 476, 95–99 (2017).

94. E. Haglund, M. Jahed, J. S. Gustavsson, A. Larsson, J. Goyvaerts, R. Baets, G. Roelkens, M. Rensing,, P. O’Brien, "High-power single transverse and polarization mode VCSEL for silicon photonics integration," Opt. Express 27, 18892-18899 (2019).

95. C. Xiang, W. Jin, J. Guo, J. D. Peters, M. J. Kennedy, J. Selvidge, P. A. Morton, J. E. Bowers, "Narrow-linewidth III-V/Si/ Si_3N_4 laser using multilayer heterogeneous integration," Optica 7, 20-21 (2020).

96. L. Agazzi, J. D. B. Bradley, M. Dijkstra, F. Ay, G. Roelkens, R. Baets, K. Wörhoff, and M. Pollnau, "Monolithic integration of erbium-doped amplifiers with silicon-on-insulator waveguides," Opt. Express 18, 27703-27711 (2010).

97. N. Li, M. Xin, Z. Su, E. S. Magden, N. Singh, J. Notaros, E. Timurdogan, P. Purnawirman, J. D. B. Bradley, and M. R. Watts, “A silicon photonic data link with a monolithic erbium-doped laser,” Sci. Rep. 10(1), 1114 (2020).

98. R. J. Mears, L. Reekie, I. M. Jauncey, and D. N. Payne, “Low-noise erbium-doped fibre amplifier operating at 1.54μm,” Electron. Lett. 23(19), 1026–1028 (1987).

99. Paschotta, J. Nilsson, A. C. Tropper, and D. C. Hanna, “Ytterbium-doped fiber amplifiers,” IEEE J. Quantum Electron. 33(7), 1049–1056 (1997).

100. M.L. Dakss and W.J. Miniscalco, “Fundamental limits on Nd^{3+}-doped fiber amplifier performance at 1.3 mm,” Photon. Technol. Lett. 2, 650 (1990).

101. E. Desurvire, J. R. Simpson, and P. C. Becker, "High-gain erbium-doped traveling-wave fiber amplifier," Opt. Lett. 12, 888-890 (1987).

102. Z. Li, A. M. Heidt, J. M. O. Daniel, Y. Jung, S. U. Alam, and D. J. Richardson, "Thulium-doped fiber amplifier for optical communications at 2 μm," Opt. Express 21, 9289-9297 (2013).

103. L. Agazzi, K. Wörhoff, and M. Pollnau, “Energy-transfer-upconversion models, their applicability and breakdown in the presence of spectroscopically distinct ion classes: A case study in amorphous Al_2O_3: Er^{3+},” J. Phys. Chem. C 117(13), 6759–6776 (2013).

104. L. Agazzi, K. Wörhoff, A. Kahn, M. Fechner, G. Huber, and M. Pollnau, “Spectroscopy of upper energy levels in an Er^{3+}-doped amorphous oxide,” J. Opt. Soc. Am. B 30(3), 663–677 (2013).

105. P. Loiko and M. Pollnau, “Stochastic model of energy-transfer processes among rare-earth ions. Example of Al_2O_3:Tm^{3+},” J. Phys. Chem. C 120(46), 26480–26489 (2016).

106. E. Magden, P. Callahan, N. Li, J. Bradley, N. Singh, A. Ruocco, L. Kolodziejski, E. Ippen, and M. R. Watts, “Frequency domain spectroscopy in rare-earth-doped gain media,” IEEE J. Quantum Electron. 24(5), 1–10 (2018).

107. J. D. B. Bradley, L. Agazzi, D. Geskus, F. Ay, K. Wörhoff, and M. Pollnau, "Gain bandwidth of 80 nm and 2 dB/cm peak gain in Al_2O_3: Er^{3+} optical amplifiers on silicon," J. Opt. Soc. Am. B 27, 187-196 (2010).

108. J. D. B. Bradley, Marcia Costa e Silva, Mathilde Gay, Laurent Bramerie, Alfred Driessen, Kerstin Wörhoff, Jean-Claude Simon, and Markus Pollnau, "170 Gbit/s transmission in an erbium-doped waveguide amplifier on silicon," Opt. Express 17, 22201-22208 (2009).

109. Sergio A. Vázquez-Córdova, Meindert Dijkstra, Edward H. Bernhardi, Feridun Ay, Kerstin Wörhoff, Jennifer L. Herek, Sonia M. García-Blanco, and Markus Pollnau, "Erbium-doped spiral amplifiers with 20 dB of net gain on silicon," Opt. Express 22, 25993-26004 (2014).

110. Jinfeng Mu, Meindert Dijkstra, Jeroen Korterik, Herman Offerhaus, and Sonia M. Garcia-Blanco, "High-gain waveguide amplifiers in Si_3N_4 technology via double-layer monolithic integration," Photon. Res. in press.

111. X. D. Fan, I. M. White, S. I. Shopova, H. Y. Zhu, J. D. Suter, and Y. Z. Sun, "Sensitive optical biosensors for unlabeled targets: A review," Anal. Chim. Acta 620, 8-26, 2008.

112. J. G. Zhu, S. K. Ozdemir, Y. F. Xiao, L. Li, L. N. He, D. R. Chen, and L. Yang, "On-chip single nanoparticle detection and sizing by mode splitting in an ultrahigh-Q microresonator," Nat. Photonics 4, 46-49 (2010).

113. L. B. Shao, X. F. Jiang, X. C. Yu, B. B. Li, W. R. Clements, F. Vollmer, W. Wang, Y. F. Xiao, and Q. H. Gong, "Detection of single nanoparticles and lentiviruses using microcavity resonance broadening," Adv Mater 25, 5616 (2013).

114. J. Su, "Label-free biological and chemical sensing using whispering gallery mode optical resonators: past, present, and future," Sensors 17(3), 540 (2017).

115. P. Steglich, M. Hulsemann, B. Dietzel, and A. Mai, "Optical Biosensors Based on Silicon-On-Insulator Ring Resonators: A Review," Molecules 24(3), 519 (2019).

116. I. M. White and X. D. Fan, "On the performance quantification of resonant refractive index sensors," Opt Express 16, 1020-1028, 2008.

117. A. J. Maker and A. M. Armani, "Heterodyned toroidal microlaser sensor," Appl Phys Lett 103, 123302 (2013).

118. N. Li, Z. Su, Purnawirman, E. S. Magden, C. V. Poulton, A. Ruocco, N. Singh, M. J. Byrd, J. D. B. Bradley, G. Leake, and M. R. Watts, "Athermal synchronization of laser source with WDM filter in a silicon photonics platform," Appl. Phys. Lett. 110, 211105 (2017).